Available online at www.sciencedirect.com

ScienceDirect

journal homepage: www.elsevier.com/locate/he

# Structural and dynamic studies of $Pr(^{11}BH_4)_3$

*Angelina Gigante* [a,b], *Seyedhosein Payandeh* [b], *Jakob B. Grinderslev* [d], *Michael Heere* [e], *Jan Peter Embs* [c], *Torben R. Jensen* [d], *Tatsiana Burankova* [c], *Arndt Remhof* [b], *Hans Hagemann* [a,*]

[a] *Département de Chimie-Physique, Université de Genève, 1211, Geneva 4, Switzerland*
[b] *Empa, Swiss Federal Laboratories for Materials Science and Technology, 8600, Dübendorf, Switzerland*
[c] *Laboratory for Neutron Scattering and Imaging, Paul Scherrer Institute, 5232, Villigen PSI, Switzerland*
[d] *Interdisciplinary Nanoscience Center (iNANO) and Department of Chemistry, Aarhus University, Langelandsgade 140, DK-8000, Aarhus C, Denmark*
[e] *Institute for Applied Materials – Energy Storage Systems (IAM – ESS), Karlsruhe Institute of Technology (KIT), Eggenstein-Leopoldshafen, Germany*

## HIGHLIGHTS

- SR-XRD confirms volume contraction at the α-Pr $(^{11}BH_4)_3$ to r-Pr $(^{11}BH_4)_3$ phase transition.
- Vibrational spectra confirm that B–H bond length do not change at this phase transition.
- QENS experiments give the activation energy for BH4 reorientation.

## GRAPHICAL ABSTRACT

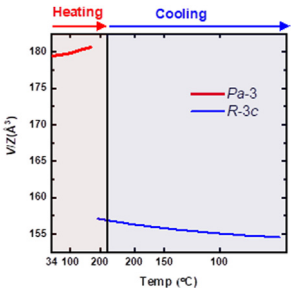


## ARTICLE INFO

*Article history:*
Received 3 May 2021
Received in revised form
23 June 2021
Accepted 29 June 2021
Available online 21 July 2021

*Keywords:*
Negative thermal expansion
Rare earth borohydrides
SR-PXD

## ABSTRACT

Rare earth borohydrides RE $(BH_4)_3$ are studied in the context of energy storage, luminescence and magnetic applications. We have investigated the structural behavior of praseodymium borohydride Pr $(^{11}BH_4)_3$ containing $^{11}B$ isotope because of the previously reported negative thermal expansion. Differential scanning calorimetry (DSC), *in-situ* variable temperature synchrotron radiation powder X-ray diffraction (SR-PXD) and infrared studies reveal that Pr $(^{11}BH_4)_3$ undergoes to a volume contraction during the phase transition from alpha α-Pr $(^{11}BH_4)_3$ to rhombohedral r-Pr $(^{11}BH_4)_3$ phase upon heating to 493 K. Surprisingly, the phase transition persists upon cooling at room temperature. Vibrational analysis also shows that the stretching frequency of $BH_4^-$ anion does not change upon heating which indicates that the B–H bond length remains constant during the structural phase transition from α-Pr $(^{11}BH_4)_3$ to r-Pr $(^{11}BH_4)_3$ phase. Additionally, the energy barrier of

* *Corresponding author.*
E-mail address: hans-rudolf.hagemann@unige.ch (H. Hagemann).
https://doi.org/10.1016/j.ijhydene.2021.06.232
0360-3199/© 2021 The Authors. Published by Elsevier Ltd on behalf of Hydrogen Energy Publications LLC. This is an open access article under the CC BY-NC-ND license (http://creativecommons.org/licenses/by-nc-nd/4.0/).

QENS
Vibrational spectroscopy

reorientation motion of the $BH_4^-$ anion in the α-phase was estimated to be ca 23 kJ/mol by quasi-elastic neutron scattering (QENS) and Raman spectroscopy.

© 2021 The Authors. Published by Elsevier Ltd on behalf of Hydrogen Energy Publications LLC. This is an open access article under the CC BY-NC-ND license (http://creativecommons.org/licenses/by-nc-nd/4.0/).

## Introduction

Rare earth borohydrides RE $(BH_4)_3$ have found to be promising materials for a variety of applications. RE $(BH_4)_3$ compounds can be used as phosphor-converted light-emitting diodes (pc-LEDs) [1–3]. For instance, $Eu(BH_4)_2$ $(THF)_2$ shows a broad blue luminescence (490 nm) with a quantum yield of 75% [1]. Further, Schouwink et al. investigated the luminescence of $Eu^{2+}$ in $RbEu(BH_4)_3$, $CsEu(BH_4)_3$ and $CsCa(BH_4)_3$:$Eu^{2+}$ occurring at 500 nm [4]. Recently, Wylezich et al. have found that the emission of $Eu^{2+}$-doped $Sr(BH_4)_{2-x}Cl_x$ and $ASr(BH_4)_{3-x}Cl_x$ (A = K, Rb, Cs) shifts strongly with temperature and could thus be used as temperature sensors [5]. The RE $(BH_4)_3$ materials have also been studied for magnetocalorimetric applications. For example, $Gd(BH_4)_3$ has a magnetic moment of $7.94\mu_B$ and paramagnetic Weiss temperature of −6.8 K, whose values are similar to the results observed by Schouwink et al. [6,7]. The lanthanides series of borohydrides have also attracted the interest as potential hydrogen storage materials due to their ability to release hydrogen in the temperature range of 473–573 K [6,8–19]. The hydrogen gravimetric density of $Yb(BH_4)_3$ and $Y(BH_4)_3$ (5.0 wt% $H_2$ and 9.1 wt% $H_2$ respectively) led to increasing research activities in these class of compounds [11,20,21]. For instance, it was found that the system $Er(BH_4)_3$–$LiBH_4$–LiH in the molar ratio 1:3:3 can undergo in the hydrogen release-uptake for three cycles by releasing 4.2, 3.7, and 3.5 wt% $H_2$ [9,22]. Rare earth borohydrides RE $(BH_4)_x$ (x = 2 or 3) are also interesting for their crystal structures. The RE $(BH_4)_3$ are found in 3 structurally related (see Fig. S1 in supplementary information) phases [9]: the α phase with space group *Pa*-3 for RE = Y, Pr, Sm, Gd, Tb, Dy, Ho, Er, Tm, Yb, the β phase with space group *Fm*-3*c* or *Pm*-3*m* for RE = Y, Pr, Sm, Ho, Er, Yb and the rhombohedral phase with space group R-3c for RE = La, Ce, Pr. In all of the mentioned structures, the RE atoms are coordinated to six $BH_4^-$ anions in an octahedral geometry and the $BH_4^-$ anions are bridging two $Re^{3+}$ cations [23–25]. The polymorphs with space group Fm-3c (cubic) have an ideal and undistorted $ReO_3$ structure, while the polymorphs with Pa-3 (cubic) and R-3c (rhombohedral) space groups assume a distorted $ReO_3$ structure.

The synthesis of RE $(BH_4)_3$ compounds can be achieved by different methods. A mechanochemically approach with precursors $LiBH_4$ and $RECl_3$, or by using solution chemistry, which generates a halide free solvated product, which can be gently heated under vacuum to obtain the pure RE $(BH_4)_3$ [6]. Recently. Payandeh et al. have discovered the negative thermal expansion [14] in $Pr(BH_4)_3$ upon heating in the temperature range of 463–473 K associated to its structural phase transitions, which precede the thermal decomposition and release of hydrogen observed around 523 K [26]. Typically, materials with negative thermal expansion [14] are characterized by a volume contraction upon heating. Some examples of NTE materials are silicates such as β-eucryptite ($LiAlSiO_4$), which shows a volume contraction of 0.15% upon heating in the temperature range 293–1073 K [27–29]. Negative thermal expansion was also observed in $ZrP_{2-x}V_xO_7$ in the temperature range 373–1073 K [30]. Mary et al. found that $ZrW_2O_8$ shows the coefficient of linear thermal expansion αL of $-9 \times 10^{-6}$ $K^{-1}$ in the temperature range of 0.3–1050 K with a volume contraction of 2.7% [31]. The NTE expansion of $ZrW_2O_8$ was attributed to the network of rigid units $WO_4$, which are dominated by strong covalent bonds and they do not expand upon heating. Since the Zr–O–W linkage are soft in $ZrW_2O_8$, the transversal oxygen atoms are displaced upon heating allowing to fill the open space in the crystal structure of $ZrW_2O_8$, which results in its NTE [31,32]. In the case of $Pr(BH_4)_3$, the authors attributed the NTE to the presence of large voids in the β-$Pr(BH_4)_3$ polymorph, which allows the increase in the Pr-B-Pr distances between $Pr(BH_4)_6$ octahedral units and the reduction of Pr–Pr distances [26]. In order to get more insight in the NTE of $Pr(BH_4)_3$, we have synthesized Pr $(^{11}BH_4)_3$ containing $^{11}B$ isotope to investigate the reason for the peculiar structural behavior of this compound. Thus, in this study, we address more details on structural and dynamic properties of Pr $(^{11}BH_4)_3$ by using a combination of synchrotron radiation powder X-ray diffraction (SR-PXD), spectroscopic investigations (quasi-elastic neutron scattering (QENS) raman, and infrared (IR) spectroscopy, and differential thermal calorimetry (DSC) study of Pr $(^{11}BH_4)_3$.

## Experimental detail

### *Synthesis of Pr($^{11}BH_4$)$_3$*

Pr $(^{11}BH_4)_3$ is synthesized according to recently published halide-free approaches, starting from metallic Pr. Pr-metal (99.9%, Alfa Aesar) was hydrogenated to form $PrH_3$ by heating to T = 673 K with a heating rate of $\Delta T/\Delta t$ = 5 K/min, in an applied hydrogen atmosphere *p* ($H_2$) = 140 bar at room temperature (RT), and subsequently cooled to RT [6,26,33]. The resulting $PrH_3$ powder was ball milled using a Fritsch Pulverisette no.6 to enhance the reactivity. $PrH_3$ was loaded into an 80 mL tungsten carbide vial together with tungsten carbide coated steel balls (diameter 10 mm) in a ball-to-powder mass ratio of 10:1, and sealed in an argon-filled glovebox ($H_2O$ and $O_2$ < 1 ppm). The ball milling program was 350 revolutions per minute (RPM) for 10min, followed by a 2min break. This sequence was repeated 10times (100min effective ball-milling time). The resulting powdered $PrH_3$ (1.5 g) was added to a 250 mL round-bottomed filter flask with a valve outlet. Dimethyl sulphide-borane ($S(CH_3)_2 \cdot {}^{11}BH_3$,

10 M, Sigma-Aldrich) was added to the powder in the molar ratio of 4.5:1 (50% excess of $S(CH_3)_2 \cdot {}^{11}BH_3$), and diluted to a 5 M solution using toluene (Sigma-Aldrich, anhydrous). The reaction mixture was left to stir at 318 K for seven days. Subsequently, the powder was dried under dynamic vacuum for 1 h at 318 K, after which the powder was washed twice with toluene (2 × 20mL) and dried for 1 h under dynamic vacuum at RT. Dimethyl sulfide ($S(CH_3)_2$) was added (80 mL) and the solution was left to stir for one day at RT, resulting in a light green solution. The reaction mixture was filtered. The filtrate was dried *in vacuo* using a rotary evaporator and subsequently dried at RT at the Schlenk line. The dry powder was transferred to Schlenk tubes and heated to 413 K for 2 h in an argon atmosphere followed by 2 h under a dynamic vacuum. This resulted in pure α-Pr $({}^{11}BH_4)_3$, confirmed by powder X-ray diffraction.

### *In-situ synchrotron radiation x-ray powder diffraction (SR-PXD) and structure refinement*

*In-situ* synchrotron radiation powder X-ray diffraction pattern (SR-PXD) of the samples were recorded at the X04SA beamline at the Swiss Light Source (SLS), Villigen, Switzerland by using a Mythen detector and a wavelength of 0.7095 Å [34]. The samples were mounted in boron silicate capillaries (o.d. 0.5–0.7 mm) and sealed with glue. The structures were refined with the Rietveld method using FullProf [35]. The backgrounds were defined based on a linear interpolation between selected points (Fig. S2) Unit cell parameters, scale factors, zero point, peak shape mixing parameters (pseudo-Voigt function), and three profile parameters (U,V,W) were refined. Fixed atomic positions and occupancies were used for the refinement.

### *Differential scanning calorimetry (DSC)*

The phase transitions of the samples were investigated by differential scanning calorimetry (DSC) using a Netzsch STA449 F3 Jupiter instrument. The samples (5–10 mg) were packed in sealed Al crucibles and the measurements were conducted with a heating ramp of 5 K/min under an argon flow of 20 mL/min.

### *Vibrational spectroscopy (IR and Raman)*

*Ex-situ* Raman experiments of Pr $({}^{11}BH_4)_3$ were conducted with LabRAM HR equipped with a confocal Raman Microscope. The Raman spectra were measured using 532 nm excitation with a CCD camera. The spectral resolution was set to 3~4 $cm^{-1}$, with an acquisition range of 120–3300 $cm^{-1}$. The Pr $({}^{11}BH_4)_3$ samples were filled in quartz capillaries (80 × 1.0 mm) in the nitrogen-filled glovebox ($H_2O$ and $O_2 < 1$ ppm) and sealed with glue. The Raman spectra were collected at 303 K. Before performing the Raman experiments of Pr $({}^{11}BH_4)_3$, two quartz capillaries were heated up to 483 K and 493 K respectively with a heating rate of 10 K/min in a Buchi Melting Point M – 565 instrument. Then, the samples were cooled to 303 K to perform *ex-situ* Raman experiments. *In-situ* variable temperature Infrared (IR) experiments of Pr $({}^{11}BH_4)_3$ were performed with a Biorad Excalibur Instrument equipped with a portable Specac Golden Gate heatable ATR setup allowing to prepare samples in the nitrogen-filled glovebox ($H_2O$, $O_2 < 1$ ppm). The spectra were recorded with a spectral resolution of 2 $cm^{-1}$, with 30scans in the range of 600–4000 $cm^{-1}$. The sample was loaded in the glovebox. The Infrared spectrum of Pr $({}^{11}BH_4)_3$ was collected at 303 K. Then, the sample was heated to 423 K, 443 K, 473 K, and 483 K to collect the IR spectra. Finally, the sample was cooled from 483–303 K to observe the spectra at 433 K, 423 K, 403 K, 363 K, and 303 K.

### *Quasielastic neutron scattering (QENS)*

Quasielastic Neutron Scattering (QENS) measurements were performed on the cold-neutron time-of-flight spectrometer FOCUS at Paul Scherrer Institute (PSI) in Switzerland with the wavelength of incident neutrons λ = 4.0 Å [36]. This experimental setup provided an energy resolution of 0.220 meV full width half maximum (FWHM) and the accessible Q-range of 0.5–2.5 $Å^{-1}$. $^{11}B$ enriched samples were used for the measurements to prevent strong neutron absorption by the $^{10}B$ isotope in natural boron. The sample containers used on FOCUS had a flat slab geometry. To minimize spectra distortion due to multiple scattering, thickness of the sample was adjusted with Al-spacers so that the sample transmission was larger than 0.90. Additional runs with a vanadium standard and an empty sample container were carried out to perform typical corrections for experimental distortions. The procedure included vanadium normalization, detector efficiency correction, and background subtraction. The sample attenuation and self-shielding factors were calculated with respect to the geometry of the experiment. The DAVE program was used for both the data reduction of the FOCUS spectra and the preliminary examination of all the data sets at individual Q-groups [37]. As the next step QENS spectra were treated in a program module, which performs two-dimensional surface fits. This approach allows for obtaining more stable and consistent results, as simultaneous fits with both E and Q being independent variables reduce the total number of free parameters to be adjusted. The summary of the studied species neutron cross-sections is provided in Table S4 in the supplementary information (SI).

## Results and discussion

### *Differential scanning calorimetry (DSC) and in-situ synchrotron radiation X-ray powder diffraction (SR-PXD) study*

Differential scanning calorimetry DSC measurements were performed to investigate the reversibility of the phase transition of Pr $({}^{11}BH_4)_3$. The DSC results are shown in Fig. 1. Two sets of experiments were performed. In the first measurement, the Pr $({}^{11}BH_4)_3$ was heated from 273–483 K (Fig. 1a), while the second measurement was performed up to 493 K (Fig. 1b). In both cases, endothermic peaks were observed in the temperature range of 463–483 K due to the phase transition of alpha α-Pr $({}^{11}BH_4)_3$ to rhombohedral r-Pr $({}^{11}BH_4)_3$. Upon cooling, exothermic signals were detected in the range 413–373 K, which were attributed to the phase transition back from rhombohedral phase r-Pr $({}^{11}BH_4)_3$ to alpha phase α-Pr

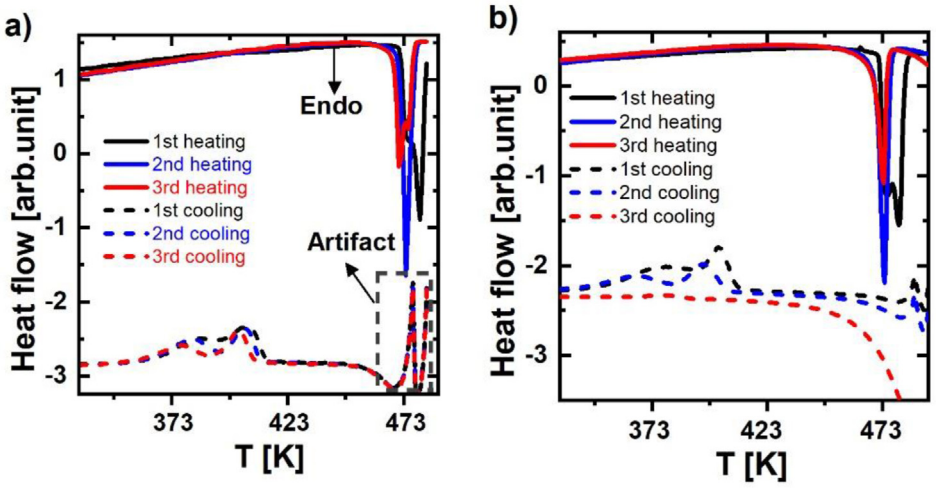


**Fig. 1 – DSC data for Pr $(^{11}BH_4)_3$ heated and cooled from 273~483 K and b) 273~493 K for three cycles. Measurements were performed under helium flow with $\Delta T/\Delta t = 5$ K/min.**

$(^{11}BH_4)_3$. In the DSC experiment performed up to 483 K (Fig. 1a), the exothermic peaks were present in all three cycles of cooling indicative of a reversible phase transition. This is also in line with the previous reports on $Pr(BH_4)_3$ [26]. However, when Pr $(^{11}BH_4)_3$ was treated up to a slightly higher temperature of 493 K (Fig. 1b), the exothermic peaks disappeared in the 3rd cooling cycle indicating of stabilization of the r-Pr $(^{11}BH_4)_3$ at room temperature (RT) and the irreversible phase transition. The irreversible phase transition was also recently observed in NTE Materials such as Guanidinium Magnesium-Hypophosphite $Mg(H_2POO)_3$] (Gua = guanidinium, $C(NH_2)_3^+$) [38,39]. Therefore, the reversibility of the phase transition from r-Pr $(^{11}BH_4)_3$ to α-Pr $(^{11}BH_4)_3$ may be related to the history and maximum temperature achieved. The highest temperature reached (*e.g.* 493 K *vs.* 483 K), as well as a longer residence time at high temperature, tends to make this transition less reversible.

The phase transition of Pr $(^{11}BH_4)_3$ was also studied by *in-situ* synchrotron powder X-ray diffraction (SP-XRD). The XRD diffraction patterns and the V/Z of Pr $(^{11}BH_4)_3$ from sequential refinements of the data are shown in Fig. 2. The Rietveld refinements of Pr $(^{11}BH_4)_3$ are reported in Fig. S2 in the supplementary information (SI). The XRD diffraction patterns of Pr $(^{11}BH_4)_3$ were collected during heating to 473 K and cooling to room temperature (RT). Fig. 2a reveals that the phase transition from cubic α-Pr $(^{11}BH_4)_3$ Pa-3 to rhombohedral r-Pr $(^{11}BH_4)_3$ R-3c phase occurs at ~458 K with the contraction of the unit cell volume (Fig. 2b). Unlike the one-step phase transition observed here, previous structural studies of $Pr(BH_4)_3$ showed a stepwise phase transition from α-phase to r-phase [26]. This negative stepwise thermal expansion passed through three cubic structures with Fm-3m space group labeled as β, β′, and β". However, in this study, no formation of cubic $Pr(BH_4)_3$ with Fm-3m space group is observed in the *in-situ* XRD, which is likely related to the physical conditions applied during $S(CH_3)_2$ removal. Moreover, unlike the former study on $Pr(BH_4)_3$ which showed a reversible phase transition, no phase transition back from r-phase (R-3c) to α-phase (Pa-3) is observed upon cooling of the sample [26]. Several reasons could be

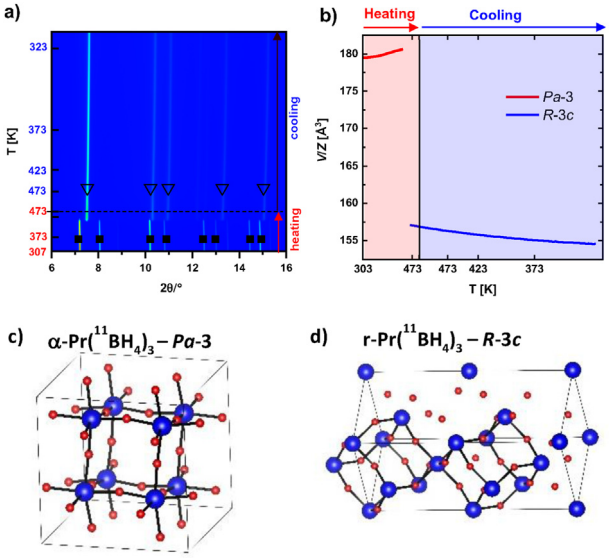


**Fig. 2 – a) *In-situ* SR-PXD data of Pr $(^{11}BH_4)_3$. Symbols: ■ α-Pr $(^{11}BH_4)_3$ Pa-3 and ▽ r-Pr $(^{11}BH_4)_3$ R-3c with $\Delta T/\Delta t = 5$ K/min ($\lambda = 0.7095$ Å) and b) V/Z (Å$^3$) evolution of Pr $(^{11}BH_4)_3$ from sequential refinements of the data. c) and d) crystal structures of α and r-Pr $(^{11}BH_4)_3$, with space groups *Pa*-3 and *R*-3c respectively. Both structures have the rhenium (vi) trioxide, $ReO_3$, structure type, and H atoms are removed for clarity. At higher temperatures, the structure is more deformed and causes the collapse of the unit cell volume. Pr, and B atoms are represented in blue in and red, and H atoms are removed for clarity. (For interpretation of the references to colour in this figure legend, the reader is referred to the Web version of this article.)**

responsible for the irreversible phase transition. One explanation is the overheating of the sample, which was observed in the DSC study of Pr $(^{11}BH_4)_3$ (Fig. 1). Secondly, the presence of $^{11}B$ isotope in Pr $(^{11}BH_4)_3$ may induce a shift in the phase transition closer to the decomposition and in most of the

cases, when the sample is over heated, it is decomposed leading to a non-reversible phase transition. The XRD of the sample before heating shows a flat background and very sharp reflections (Fig. S2a), but the reduced intensities of the XRD pattern after heating and the modulated background, suggest an amorphous phase as the decomposition product (Fig. S2b).

### *Infrared (IR) and Raman study*

Fig. 3a shows the room temperature (RT) infrared spectrum (black spectrum) and Raman spectrum (red spectrum) of the α-Pr ($^{11}BH_4)_3$ phase. The room temperature IR spectrum shows two $BH_4^-$ deformation bands at 1119 and 1168 $cm^{-1}$ (total splitting 49 $cm^{-1}$), and a single B–H stretching mode centered at 2250 $cm^{-1}$ as shown in the black spectrum in Fig. 3a. The room temperature IR and Raman spectra of α-Pr ($^{11}BH_4)_3$ in the Pa-3 phase resemble to those reported previously for $Y(BH_4)_3$ [21]. The Raman spectrum reveals a significant splitting of the B–H stretching modes around 2300 $cm^{-1}$, which reflect the presence of significant Fermi resonances (red spectrum in Fig. 3a) [40]. In the bending mode region, the modes originating from the $\nu_2$ mode with E symmetry (around 1300 $cm^{-1}$) for the perfect tetrahedron are extremely weak in the IR spectrum, confirming that the $BH_4^-$ ions are isolated and do not act as complexing ions for the $Pr^{3+}$ ion [41,42].

Sato et al. have also studied theoretically the structures and vibrational spectra of $M(BH_4)_3$ (M = Y, Dy and Gd) in the Pa-3 phase [44]. The Raman spectrum of Pr ($^{11}BH_4)_3$ is similar to the calculated Raman active vibrations for $Gd(BH_4)_3$ which are shown in Table S1 in the SI. The symmetry analysis of the vibrations of α-Pr ($^{11}BH_4)_3$ in the Pa-3 phase are reported in Table S2 of the SI. The calculated stretching Raman frequencies (in the harmonic approximation) are all centered close to 2280 $cm^{-1}$, confirming that all B–H bond lengths have practically the same value as shown in Fig. S3 in the SI. On the other side, the frequencies of the $\nu_2$ and $\nu_4$ deformation modes are spread over a wide range. This indicates a low local symmetry for Pr ($^{11}BH_4)_3$. Sato et al. report calculated H–B–H angles ranging from 107° to 113° for $Gd(BH_4)_3$. The spread of the calculated vibrational frequencies of the $\nu_2$ and $\nu_4$ deformation modes also reveal the presence of significant factor group splitting (*e.g.* coupling of vibrations of adjacent $BH_4^-$ ions). The highest frequency lattice mode is observed at 603 $cm^{-1}$ in the RT Raman spectrum of Pr ($^{11}BH_4)_3$ (red spectrum in Fig. 3b), which corresponds to the highest energy librational mode of the $BH_4^-$ anion. Typically, the frequencies of the librational modes are higher than the translational lattice modes, however couplings may occur. Fig. 3 indicates that the librational modes are mostly located between 359 and 603 $cm^{-1}$, which is also comparable with the calculated vibrational spectra for $Gd(BH_4)_3$ [44]. The frequency of librational modes can be related to the barrier of reorientation using the approximation of the Mathieu equation. The energy barrier of reorientation motion of the $BH_4^-$ anion 'V' can be obtained according to Equation (1) [45,46]:

$$V = \frac{\pi^2 \cdot I \cdot \nu^2}{2}\left(1 + \frac{h}{2 \cdot \pi^2 \cdot I \cdot \nu}\right)^2 \quad (1)$$

where: $\nu$ is the frequency of the librational mode associated to $BH_4$ and $I$ is the moment of inertia of $BH_4^-$. ($I$ is fixed and given by the B–H bond length, h is the Planck constant). For $\nu = 603\ cm^{-1}$ and $\nu = 359\ cm^{-1}$, energy barriers of V = 65 kJ/mol and V = 23 kJ/mol can be estimated respectively, using a B–H bond length of 1.22 Å. For a better understanding of the effect of the heating on the vibrational modes of $BH_4^-$ anion, we have performed *ex-situ* Raman experiments at 303 K in the range of 120-3300 $cm^{-1}$ (see Fig. 3b). Two quartz capillaries containing Pr ($^{11}BH_4)_3$ were subjected to two different experiments. One capillary was heated to 483 K and a second capillary up to 493 K in a melting point machine with a heating rate of 10 K/min. Then, the samples were cooled down at 303 K to collect *ex-situ* Raman spectra The low-frequency spectra (below 700 $cm^{-1}$) show different features when Pr ($^{11}BH_4)_3$ is cooled from 493 K to 483–303 K (Fig. 3b). Thus, this may suggest that the irreversibility of the phase transition upon cooling of Pr ($^{11}BH_4)_3$ as also observed in DSC and SR-PXD experiments. Group theory predicts much fewer Raman active modes on

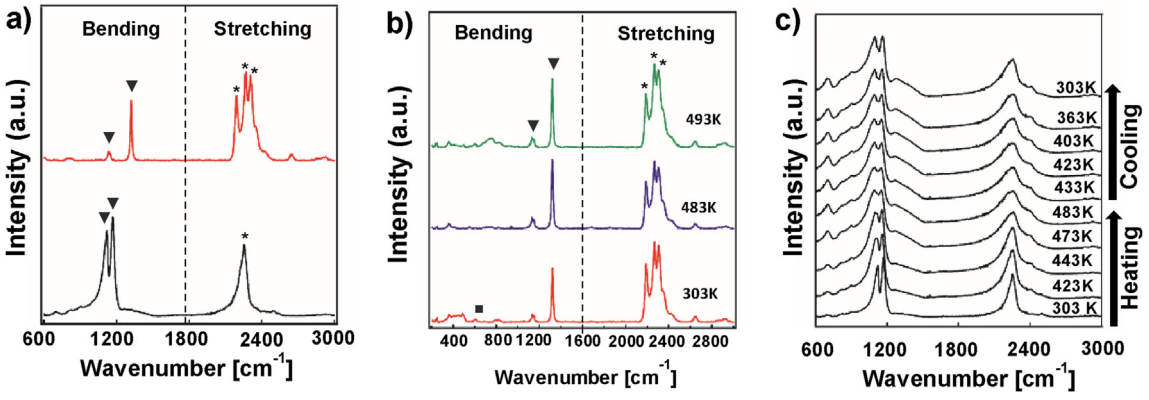


**Fig. 3 – a) IR (black) and Raman (red) spectra of α-Pr ($^{11}BH_4)_3$ at 303 K. b) *In-situ* variable temperature IR spectra of Pr ($^{11}BH_4)_3$. b) *Ex-situ* Raman spectra of Pr ($^{11}BH_4)_3$ at 303 K before heating [43], after heating at 483 K (purple), after heating at 493 K (green). c) *In-situ* variable temperature IR spectra of Pr ($^{11}BH_4)_3$. Symbols: ▼ IR and Raman bending modes, ∗ IR and Raman stretching modes, ■ Raman librational mode. (For interpretation of the references to colour in this figure legend, the reader is referred to the Web version of this article.)**

this spectral region for the r-Pr $(^{11}BH_4)_3$ phase (R-3c) (see Table S3 in SI). To get information about the reversibility of the phase transition of Pr $(^{11}BH_4)_3$ upon cooling, *in-situ* variable temperature IR experiments were performed, and the results are shown in Fig. 3c. During heating, the phase transition from α-Pr $(^{11}BH_4)_3$ to r-Pr $(^{11}BH_4)_3$ phase is observed at 473 K, and it appears irreversible upon cooling as shown in Fig. 3c. In the r-Pr $(^{11}BH_4)_3$, the splitting of the $\nu_4$ deformation band increases to 63 $cm^{-1}$ (vs. 49 $cm^{-1}$ in the α-Pr $(^{11}BH_4)_3$ phase as previously discussed in this section), suggesting an increased angular deformation [41]. The RE $(BH_4)_3$ compounds can crystallize in $ReO_3$ type structure [23], few compounds based on $ReO_3$ type structure show negative thermal expansion upon heating [25]. Literature results show that for this type of compounds, the frequencies of the longitudinal vibrations increase during the heating while the frequencies of the transverse vibrations perpendicular to the direction of the atom chain decrease upon heating. This phenomenon is associated to the volume contraction and therefore to the NTE in which the $MO_4$ tetrahedra remain rigid and they are connected by cover sharing the oxygen atoms [25,47–49]. In the case of Pr $(^{11}BH_4)_3$, the stretching frequency of $BH_4^-$ remains almost constant, implying that the B–H bond length has not changed significantly by the structural phase transition from α-Pr $(^{11}BH_4)_3$ to r-Pr $(^{11}BH_4)_3$ phase despite the significant lattice contraction observed by SR-PXD experiment previously discussed. Additionally, the increased splitting of the $\nu_4$ band suggests a stronger deformation of the $BH_4^-$ ion in the r-Pr $(^{11}BH_4)_3$ phase.

### *Quasielastic neutron scattering (QENS) study*

Temperature-dependent quasielastic neutron scattering (QENS) experiments of Pr $(^{11}BH_4)_3$ were performed upon heating and cooling. The scattering intensity of Pr $(^{11}BH_4)_3$ is dominated by the incoherent component associated with single-particle dynamics of the borohydride units, as shown in Table S4 in the SI. The analysis is described in SI (Equations S1 to S3) and the results of the analysis is presented in Figs. 5–7. Each spectrum has been fitted with Equations (S1⊗S3)⊗R (Q,E) (⊗ denotes convolution) taking into account the instrumental resolution R (Q,E). From the Q-dependence we determined the mean-square displacement (msd), the residence time of the reorientational motion and

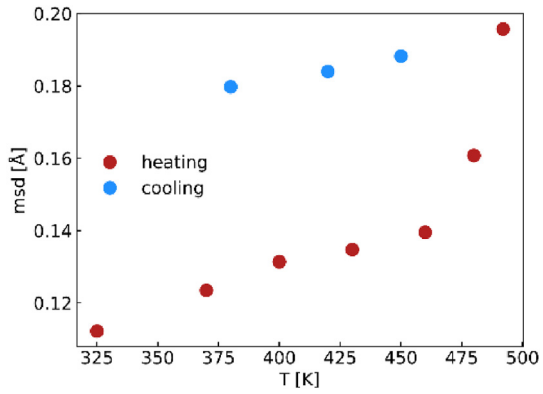


**Fig. 5 – Temperature dependence of the mean square displacement (msd) associated with the low-frequency vibrational modes (overdamped librations, vibrations). A rapid increase in the msd starting at 480 K is due to the broadening and the shift of the inelastic feature at 7.5 meV in Fig. 4. The disorder induced by the phase transition is preserved on cooling leading to larger msd-values on cooling as compared to the heating cycle.**

the linewidth of the overdamped vibrational dynamics for a given (fixed) temperature. The fit-function has been chosen to describe the possible dynamical processes compatible with the geometry of the corresponding molecules. Assuming that the energy scale for rotations and vibrations differs significantly, the dynamic structure factor $S_{BH4}(Q,E)$ can be defined as a convolution of two individual scattering functions, representing vibrational and stochastic localized motions as shown in SI. The spectra in the quasielastic energy range and the fits to the model function are presented in Fig. 4. It is necessary to mention that the rotational component's linewidths are quite narrow ~20 μeV at T = 430 K relatively to the resolution function (HWHM = 110 μeV), and the exact geometry of reorientations is challenging to infer. The temperature dependence of the fit parameters is displayed in Figs. 4–7.

Fig. 5 shows the temperature dependence of the mean square displacement (msd) associated with the low-frequency vibrational modes (overdamped librations, vibrations). A rapid increase in the msd starting at 480 K is due to the broadening and the shift of the inelastic feature at 7.5 meV seen in Fig. S4

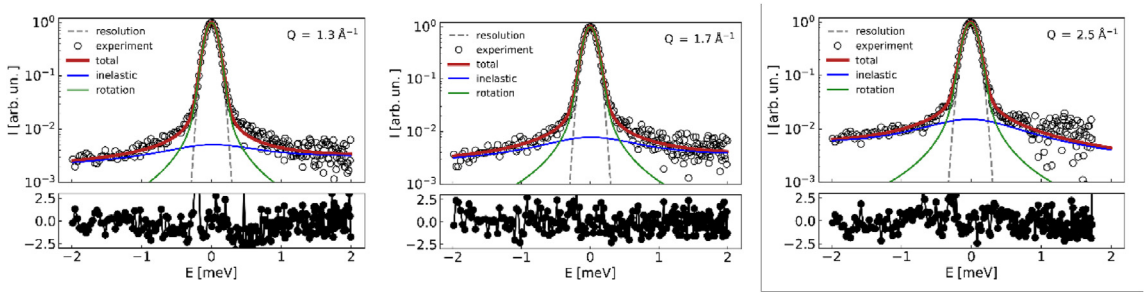


**Fig. 4 – Experimental spectra of $Pr(BH_4)_3$ at selected Q-values and T = 430 K. The lines in the plots are the total fit curve [43], rotational contribution (green), and low-energy inelastic contribution (blue). The solid black dots present the residuals of the difference between the measured data and the fit function. (For interpretation of the references to colour in this figure legend, the reader is referred to the Web version of this article.)**

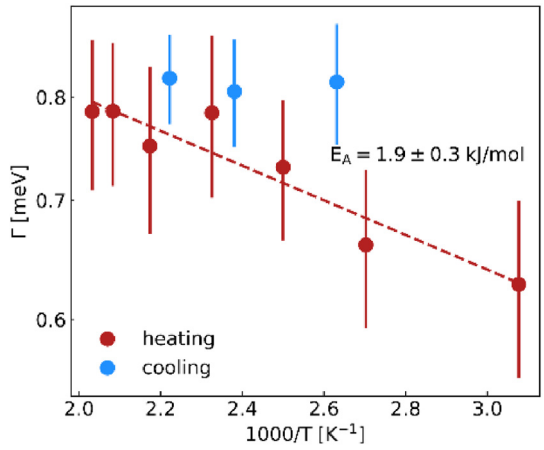


**Fig. 6 – Linewidths of the overdamped vibrational component as a function of the temperature. On heating, the temperature dependence demonstrates an Arrhenius behavior with the activation energy of 1.9 ± 0.3 kJ/mol. The disorder induced by the phase transition is preserved on cooling leading to broader quasielastic lines at the same temperatures as compared to the heating cycle.**

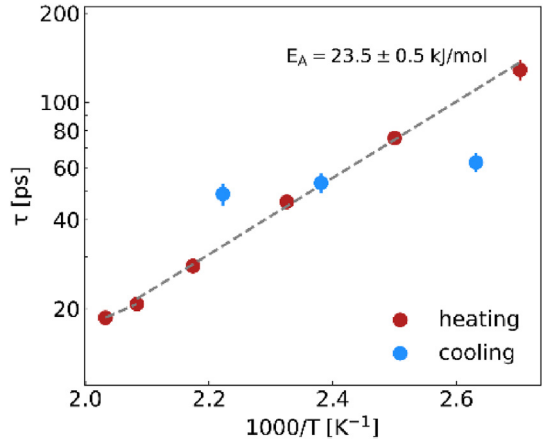


**Fig. 7 – Residence time of the C2/C3 reorientational motion of the borohydride units as a function of temperature. On average the temperature dependence follows the law of Arrhenius with the activation energy of 23.5 ± 0.5 kJ/mol. An enhancement of rotational dynamics at 480 K concurrent with the enhancement of the vibrational components is hard to detect due to the narrow linewidths. The residence times at low temperatures are estimated with big errors and not reliable. Here there might be a change in activation energy between 460 and 480 K (see figure below). Measurement with a finer resolution function are necessary to prove this.**

in SI. The disorder induced by the phase transition is preserved on cooling leading to larger msd-values on cooling as compared to the heating cycle. Fig. 6 represents the linewidths of the overdamped vibrational component as a function of temperature. On heating, the temperature dependence demonstrates an Arrhenius behavior with the activation energy of 1.9 ± 0.3 kJ/mol according to Equation (2):

$$\frac{\Gamma}{\Gamma_0} = \exp\left(-\frac{E_a}{k_B T}\right) \quad (2)$$

where $\Gamma$ is the linewidths of the overdamped vibrational component. $\Gamma_0$ is a prefactor. $E_a$ is the activation energy. $k_B$ is the Boltzmann constant and $T$ is the temperature. The disorder induced by the phase transition is preserved on cooling leading to broader quasielastic lines at the same temperatures as compared to the heating cycle. Fig. 7 represents the residence time of the C2/C3 reorientational motion of the borohydride units as a temperature function. On average, the temperature dependence follows Arrhenius' law according to Equation (3) with the activation energy of 23.5 ± 0.5 kJ/mol as shown in Fig. 7.

$$\frac{\tau}{\tau_0} = \exp\left(-\frac{E_a}{k_B T}\right) \quad (3)$$

where $\tau$ is the residence time of the C2/C3 reorientational motion of the borohydride units. $\tau_0$ is a prefactor. $E_a$ is the activation energy. $k_B$ is the Boltzmann constant and $T$ is the temperature. For $Y(BH_4)_3$, NMR studies have revealed two jump processes for the $BH_4^-$ group in the α phase with activation energies of 32.5 and 19.3 kJ/mol, respectively [50]. Considering the significantly smaller unit cell of $Y(BH_4)_3$ compared to $Pr(BH_4)_3$, the motion corresponding to the value of $E_A = 32.5$ kJ/mol for $Y(BH_4)_3$ could correspond to the value of $E_A = 23.5$ kJ/mol obtained here for Pr $(^{11}BH_4)_3$. Further, the activation energy obtained from Arrhenius law is in agreement with the energy barrier previously discussed in the vibrational section. Therefore, in the significantly smaller rhombohedral phase, at least one re-orientational barrier for the $BH_4^-$ ion becomes much lower. The associated gain in entropy might be the driving force for the collapse of the structure and the negative thermal expansion.

## Conclusions

The new studies with $^{11}B$ labeled $Pr(BH_4)_3$ did not allow to reproduce the unique negative thermal expansion of successive β phases observed in our first study. The *in-situ* IR experiments show that the B–H bond length remains practically unchanged from the cubic α to the rhombohedral phase, despite the significant lattice contraction. The increased splitting of the $\nu_4$ band suggests a stronger deformation of the $BH_4^-$ ion in the rhombohedral phase. Finally, the QENS data show for the α phase a $BH_4$ reorientational barrier of ca 23.5 kJ/mol. The surprising result is thus that in the significantly smaller rhombohedral phase, at least one reorientational barrier for the $BH_4^-$ ion becomes much lower, while the size of this ion remains practically unchanged between the α and the rhombohedral phase. Whether this motion is associated to the decomposition and hydrogen release observed at 523 K remains to be established.

## Supplementary information

Supporting characterization data are provided: SR-PXD, IR, Raman, QENS.

## Declaration of competing interest

The authors declare that they have no known competing financial interests or personal relationships that could have appeared to influence the work reported in this paper.

## Acknowledgements

This work was supported in part by the Swiss National Science Foundation, Switzerland (projects 200021-169033 and 200020_182494). MH acknowledges the project "Energy Research with Neutrons (ErwiN)", which is funded by the German Federal Ministry of Education and Research (BMBF) [51]. NordForsk and The Nordic Neutron Science Program, FunHy (Project no. 81942) and The Independent Research Fund Denmark for technology and production (HyNanoBorN, DFF – 4181–00462) are acknowledged for funding. The EMPAPOSTDOCS-II program has received funding from the European Union's Horizon 2020 research and innovation program under the Marie Skłodowska-Curie grant agreement number 754364. We acknowledge the Paul Scherrer Institute in Villigen, Switzerland, for provision of synchrotron radiation beamtime at the MS-X04SA beamline of the Swiss Light Source (SLS), and we would like to thank Nicola Casati for assistance.

## Appendix A. Supplementary data

Supplementary data to this article can be found online at https://doi.org/10.1016/j.ijhydene.2021.06.232.

## REFERENCES

[1] Marks S, Heck JG, Habicht MH, Oña-Burgos P, Feldmann C, Roesky PW. $[Ln(BH_4)_2(THF)_2]$ (Ln = Eu, Yb)—a highly luminescent material. Synthesis, properties, reactivity, and NMR studies. J Am Chem Soc 2012;134:16983–6.

[2] Sharma M, Didelot E, Spyratou A, Lawson Daku LM, Černý R, Hagemann H. Halide free $M(BH_4)_2$ (M=Sr, Ba, and Eu) synthesis, structure, and decomposition. Inorg Chem 2016;55:7090–7.

[3] Christmann J, Mansouri A, Grinderslev JB, Jensen TR, Hagemann H. Probing the local symmetry of $Tb^{3+}$ in borohydrides using luminescence spectroscopy. J Lumin 2020;221:117065.

[4] Schouwink P, Ley MB, Tissot A, Hagemann H, Jensen TR, Smrčok Ľ, et al. Structure and properties of complex hydride perovskite materials. Nat Commun 2014;5:5706.

[5] Wylezich T, Sontakke AD, Castaing V, Suta M, Viana B, Meijerink A, et al. One ion, many facets: efficient, structurally and thermally sensitive luminescence of $Eu^{2+}$ in binary and ternary strontium borohydride chlorides. Chem Mater 2019;31:8957–68.

[6] Grinderslev JB, Møller KT, Bremholm M, Jensen TR. Trends in synthesis, crystal structure, and thermal and magnetic properties of rare-earth metal borohydrides. Inorg Chem 2019;58:5503–17.

[7] Schouwink P, Didelot E, Lee Y-S, Mazet T, Černý R. Structural and magnetocaloric properties of novel gadolinium borohydrides. J Alloys Compd 2016;664:378–84.

[8] Grinderslev JB, Ley MB, Lee Y-S, Jepsen LH, Jørgensen M, Cho YW, et al. Ammine lanthanum and cerium borohydrides, $M(BH_4)_3 \cdot nNH_3$; trends in synthesis, structures, and thermal properties. Inorg Chem 2020;59:7768–78.

[9] Frommen C, Sørby MH, Heere M, Humphries TD, Olsen JE, Hauback BC. Rare earth borohydrides—crystal structures and thermal properties. Energies 2017;10:2115.

[10] Hagemann H. Estimation of thermodynamic properties of metal hydroborates. Chemistry 2019;4:8989–92.

[11] Olsen JE, Frommen C, Sørby MH, Hauback BC. Crystal structures and properties of solvent-free $LiYb(BH_4)_4–xCl_x$, $Yb(BH_4)_3$ and $Yb(BH_4)_2–xCl_x$. RSC Adv 2013;3:10764–74.

[12] Frommen C, Aliouane N, Deledda S, Fonneløp JE, Grove H, Lieutenant K, et al. Crystal structure, polymorphism, and thermal properties of yttrium borohydride $Y(BH_4)_3$. J Alloys Compd 2010;496:710–6.

[13] Grinderslev JB, Jensen TR. Trends in the series of ammine rare-earth-metal borohydrides: relating structural and thermal properties. Inorg Chem 2021;60:2573–89.

[14] Bannenberg L, Heere M, Benzidi H, Montero J, Dematteis E, Suwarno S, et al. Metal (boro-) hydrides for high energy density storage and relevant emerging technologies. Int J Hydrogen Energy 2020;45:33687–730.

[15] Milanese C, Jensen TR, Hauback B, Pistidda C, Dornheim M, Yang H, et al. Complex hydrides for energy storage. Int J Hydrogen Energy 2019;44:7860–74.

[16] Huang T, Zou J, Zeng X, Wang J, Liu H, Ding W. Reversible hydrogen sorption behaviors of the $3NaBH_{4-(x)}$ $YF_{3-(1-x)}$ $GdF_3$ system: the effect of double rare earth metal cations. Int J Hydrogen Energy 2019;44:4868–77.

[17] Heere M, GharibDoust SP, Sørby MH, Frommen C, Jensen TR, Hauback BC. In situ investigations of bimetallic potassium erbium borohydride. Int J Hydrogen Energy 2017;42:22468–74.

[18] Abdelhamid HN. A review on hydrogen generation from the hydrolysis of sodium borohydride. Int J Hydrogen Energy 2020;46:726–65.

[19] Wegner W, Jaroń T, Grochala W. Polymorphism and hydrogen discharge from holmium borohydride, $Ho(BH_4)_3$, and $KHo(BH_4)_4$. Int J Hydrogen Energy 2014;39:20024–30.

[20] Heere M, GharibDoust SHP, Brighi M, Frommen C, Sørby MH, Černý R, et al. Hydrogen sorption in erbium borohydride composite mixtures with $LiBH_4$ and/or LiH. Inorganics 2017;5:31.

[21] Jaroń T, Grochala W. $Y(BD_4)_3$, an efficient store of deuterium, and impact of isotope effects on its thermal decomposition. J Nucl Mater 2012;420:307–13.

[22] Heere M, Payandeh GharibDoust SH, Frommen C, Humphries TD, Ley MB, Sørby MH, et al. The influence of LiH on the rehydrogenation behavior of halide free rare earth (RE) borohydrides (RE=Pr, Er). Phys Chem Chem Phys 2016;18:24387–95.

[23] Hadjixenophontos E, Dematteis EM, Berti N, Wołczyk AR, Huen P, Brighi M, et al. A review of the MSCA ITN ECOSTORE—novel complex metal hydrides for efficient and compact storage of renewable energy as hydrogen and electricity. Inorganics 2020;8:17.

[24] Paskevicius M, Jepsen LH, Schouwink P, Černý R, Ravnsbæk DB, Filinchuk Y, et al. Metal borohydrides and derivatives – synthesis, structure and properties. Chem Soc Rev 2017;46:1565–16634.

[25] Evans HA, Wu Y, Seshadri R, Cheetham AK. Perovskite-related $ReO_3$-type structures. Nat Rev Mater 2020;5:196–213.

[26] Payandeh GharibDoust S, Heere M, Nervi C, Sørby MH, Hauback BC, Jensen TR. Synthesis, structure, and polymorphic transitions of praseodymium(iii) and neodymium(iii) borohydride, $Pr(BH_4)_3$ and $Nd(BH_4)_3$. Dalton Trans 2018;47:8307–19.

[27] Gillery F, Bush E. Thermal contraction of β-eucryptite-.($Li_2O.Al_2O_3.2SiO_2$) by X-ray and dilatometer methods. J Am Ceram Soc 1959;42:175–7.
[28] Takenaka K. Negative thermal expansion materials: technological key for control of thermal expansion. Sci Technol Adv Mater 2012;13:1–11.
[29] Takenaka K. Progress of research in negative thermal expansion materials: paradigm shift in the control of thermal expansion. Front Chem 2018;6:267.
[30] Korthuis V, Khosrovani N, Sleight A, Roberts N, Dupree R, Warren WJ. Negative thermal expansion and phase transitions in the $ZrV_{2-x}P_xO_7$ series. Chem Mater 1995;7:412–7.
[31] Mary T, Evans J, Vogt T, Sleight A. Negative thermal expansion from 0.3 to 1050 Kelvin in $ZrW_2O_8$. Science 1996;272:90–2.
[32] Evans J. Negative thermal expansion materials. J Chem Soc, Dalton Trans 1999;19:3317–26.
[33] Richter B, Grinderslev JB, Møller KT, Paskevicius M, Jensen TR. From metal hydrides to metal borohydrides. Inorg Chem 2018;57:10768–80.
[34] Bergamaschi A, Cervellino A, Dinapoli R, Gozzo F, Henrich B, Johnson I, et al. The MYTHEN detector for X-ray powder diffraction experiments at the Swiss Light Source. J Synchrotron Radiat 2010;17:653–68.
[35] Roisnel T, Rodriguez-Carvajal J. Computer program FULLPROF. LLB-LCSIM; May. 2003.
[36] Mesota J, Janssen S, Holitzner L, Hempelmann R. Focus: project of a space and time focussing time-of-flight spectrometer for cold neutrons at the spallation source SINQ of the Paul scherrer institute. J Neutron Res 1996;3:293–310.
[37] Azuah RT, Kneller LR, Qiu Y, Tregenna-Piggott PL, Brown CM, Copley JR, et al. DAVE: a comprehensive software suite for the reduction, visualization, and analysis of low energy neutron spectroscopic data. J Res Nat Inst Stand Technol 2009;114:341–58.
[38] Long J, Basalov IV, Lyssenko KA, Cherkasov AV, Mamontova E, Guari Y, et al. Synthesis, structure, magnetic and photoluminescent properties of dysprosium (III) Schiff Base single-molecule magnets: investigation of the relaxation of the magnetization. Chem - Asian J 2020;15:2706–15.
[39] Gao H-Q, Wei W-J, Tan Y-H, Tang Y-Z. Phase transition and negative thermal expansion in guanidinium magnesium-hypophosphite hybrid perovskite. Chem Mater 2020;32:6886–91.
[40] Carbonnière P, Hagemann H. Fermi resonances of borohydrides in a crystalline environment of alkali metals. J Phys Chem 2006;110:9927–33.
[41] D'Anna V, Lawson Daku LM, Hagemann H. Quantitative spectra–structure relations for borohydrides. J Phys Chem C 2015;119:21868–74.
[42] D'Anna V, Spyratou A, Sharma M, Hagemann H. FT-IR spectra of inorganic borohydrides. Spectrochim Acta Mol Biomol Spectrosc 2014;128:902–6.
[43] Arbaoui A, Redshaw C. Metal catalysts for ε-caprolactone polymerisation. Polym Chem 2010;1:801–26.
[44] Sato T, Miwa K, Nakamori Y, Ohoyama K, Li H-W, Noritake T, et al. Experimental and computational studies on solvent-free rare-earth metal borohydrides $R(BH_4)_3$ (R=Y, Dy, and Gd). Phys Rev B 2008;77:104114.
[45] Hagemann H, Gomes S, Renaudin G, Yvon K. Raman studies of reorientation motions of [BH4]− anionsin alkali borohydrides. J Alloys Compd 2004;363:129–32.
[46] Hagemann H, Filinchuk Y, Chernyshov D, van Beek W. Lattice anharmonicity and structural evolution of $LiBH_4$: an insight from Raman and X-ray diffraction experiments. Phase Transitions 2009;82:344–55.
[47] Ernst G, Broholm C, Kowach G, Ramirez A. Phonon density of states and negative thermal expansion in $ZrW_2O_8$. Nature 1998;396:147–9.
[48] Lind C. Two decades of negative thermal expansion research: where do we stand? Materials 2012;5:1125–54.
[49] Attfield JP. Mechanisms and materials for NTE. Front Chem 2018;6:371.
[50] Soloninin AV, Skripov AV, Yan Y, Remhof A. Nuclear magnetic resonance study of hydrogen dynamics in $Y(BH_4)_3$. J Alloys Compd 2013;555:209–12.
[51] Heere M, Mühlbauer MJ, Schökel A, Knapp M, Ehrenberg H, Senyshyn A. Energy research with neutrons (ErwiN) and installation of a fast neutron powder diffraction option at the MLZ, Germany. J Appl Crystallogr 2018;51:591–5.